

## RESEARCH ARTICLE

10.1002/2017JC013251

## Key Points:

- The first synchronously coupled, fully conservative ice shelf-ocean model has been developed
- Unlike a simple parameterized melt simulation, coupled runs have asymmetric ice-shelf topography
- For a given ice-shelf mass, parameterizing melt tends to underestimate ice-shelf buttressing

## Supporting Information:

- Video S1
- Video S2
- Video S3

## Correspondence to:

J. R. Jordan,  
jamrda26@bas.ac.uk

## Citation:

Jordan, J. R., Holland, P. R., Goldberg, D., Snow, K., Arthern, R., Campin, J.-M., . . . Jenkins, A. (2018). Ocean-forced ice-shelf thinning in a synchronously coupled ice-ocean model. *Journal of Geophysical Research: Oceans*, 123, 864–882. <https://doi.org/10.1002/2017JC013251>

Received 6 JUL 2017

Accepted 5 OCT 2017

Accepted article online 27 OCT 2017

Published online 3 FEB 2018

## Ocean-Forced Ice-Shelf Thinning in a Synchronously Coupled Ice-Ocean Model

James R. Jordan<sup>1</sup> , Paul R. Holland<sup>1</sup>, Dan Goldberg<sup>2</sup>, Kate Snow<sup>2</sup>, Robert Arthern<sup>1</sup> , Jean-Michel Campin<sup>3</sup> , Patrick Heimbach<sup>4</sup>, and Adrian Jenkins<sup>1</sup> 

<sup>1</sup>British Antarctic Survey, Research Institute in Cambridge, Cambridge, UK, <sup>2</sup>School of GeoSciences, University of Edinburgh, Edinburgh, UK, <sup>3</sup>Department of Earth, Atmospheric and Planetary Sciences, Massachusetts Institute of Technology, Cambridge, MA, USA, <sup>4</sup>Institute for Computational Engineering and Science, University of Texas at Austin, Austin, TX, USA

**Abstract** The first fully synchronous, coupled ice shelf-ocean model with a fixed grounding line and imposed upstream ice velocity has been developed using the MITgcm (Massachusetts Institute of Technology general circulation model). Unlike previous, asynchronous, approaches to coupled modeling our approach is fully conservative of heat, salt, and mass. Synchronous coupling is achieved by continuously updating the ice-shelf thickness on the ocean time step. By simulating an idealized, warm-water ice shelf we show how raising the pycnocline leads to a reduction in both ice-shelf mass and back stress, and hence buttressing. Coupled runs show the formation of a western boundary channel in the ice-shelf base due to increased melting on the western boundary due to Coriolis enhanced flow. Eastern boundary ice thickening is also observed. This is not the case when using a simple depth-dependent parameterized melt, as the ice shelf has relatively thinner sides and a thicker central “bulge” for a given ice-shelf mass. Ice-shelf geometry arising from the parameterized melt rate tends to underestimate backstress (and therefore buttressing) for a given ice-shelf mass due to a thinner ice shelf at the boundaries when compared to coupled model simulations.

## 1. Introduction

Melting beneath floating ice shelves, which accounts for roughly half of the freshwater flux from Antarctica (Depoorter et al., 2013), takes place where sufficiently warm ocean water makes contact with the ice-shelf base. Cooling of continental shelf waters by sea ice growth protects much of the Antarctic margin from the warm Circumpolar Deep Water (CDW) of the Southern Ocean (Jacobs et al., 1992). However, in some locations of both the West Antarctic Ice Sheet (WAIS) (Dutrieux et al., 2014; Petty et al., 2013; Walker et al., 2007) and East Antarctic Ice Sheet (EAIS) (Greenbaum et al., 2015; Silvano et al., 2016), deep ocean troughs and weaker ice growth allow warm CDW to infiltrate the continental shelf. Where this occurs, melt rates can reach tens of meters per year or higher (Jacobs et al., 1996).

The mechanism by which this melting affects sea level rise is indirect, since thinning of ice shelves has negligible direct contribution. Rather, thinning of an ice shelf affects the restraining force (often termed “buttressing”) that the ice shelf provides to the ice sheet that feeds it (Dupont & Alley, 2005). With a lessening of this restraint, ice would flow into the ocean at a greater rate and there might be retreat of the grounded ice sheet extent, or grounding line (Thomas et al., 1979).

Buttressing is provided by slow-moving ice at the side margins of embayed ice shelves, or by “pinning points” (areas of grounded ice within the ice shelf) (Thomas, 1979). Strong increases in seaward grounded ice fluxes have been observed as a result of ice-shelf thinning (Shepherd et al., 2004) and disintegration (Scambos et al., 2004). Improved understanding of the response of ice sheets to ice-shelf thinning is therefore vital to constraining future behavior of the Antarctic Ice Sheet under differing climate scenarios. Attempts to quantify this response are complicated, however, by the possibility of feedbacks within the ice-ocean system.

Our understanding of the dynamics of coupled ice-ocean behavior is hampered by the lack of existing models that can suitably represent ice-ocean interactions (Joughin et al., 2012). Ocean models have difficulties

accounting for continuously changing ice-margin geometry, and ice models are only now approaching a level at which interactions between floating and grounded ice can be correctly represented (Favier et al., 2014; Pattyn & Durand, 2013).

In this work, we present the first truly synchronous, coupled ice shelf-ocean model and use it to investigate the effects of ocean temperature variation on ice-shelf buttressing. The coupled model is described, along with the process of online adaptation of the ice-ocean boundary. We also compare our coupled results to an ice model forced by a simple depth-dependent parameterized melt rate, and compare the effects upon buttressing of the two methods.

## 2. Approaches to Coupled Modeling

Ice shelf-ocean coupling can be approached in a number of ways that fall into three broad categories, which we refer to as “discontinuous,” “asynchronous,” and “synchronous” coupling. While describing these approaches, we refer to the time step of both the ocean and ice components of the coupled model as well as a separate, coupled time step. This coupled time step is defined to be the interval between the exchange of melt rate and ice-shelf thickness between the ice and ocean models.

“Discontinuous” coupling initializes a new ocean model every one or few ice time steps, with each new ocean model having a different ice-shelf geometry. The coupled time step is therefore of the order of the ice time step. The ocean model is spun-up from suitable initial conditions and fixed boundary conditions, and then the steady state ocean melt rate is used in the continuously running ice model for the entire next coupled time step. From a practical standpoint, this approach tends to be very easy to implement, as the coupling process is all done offline using the existing model initialization code. This approach is potentially computationally cheap (assuming the ocean spin-up time is noticeably smaller than the coupled time step), with the expensive ocean model run time kept to a minimum as it is not running continuously (although spin-up time between coupled time steps is required). However, as the ocean history is discarded for each new initialization, the coupled model does not conserve heat, salt and mass between coupled time steps. This approach cannot be used with rapidly varying forcings because the ocean model history must be maintained in these circumstances. It also cannot be used in global coupled climate models (GCMs), which cannot repeatedly spin-up their ocean model. Examples of models that use this approach are Goldberg et al. (2012a, 2012b), Gladish et al. (2012), and De Rydt and Gudmundsson (2016).

In “asynchronous” coupling both the ice and ocean models are run simultaneously, exchanging information between them every one or few ice time steps. The coupled time step is therefore similar to that of a discontinuous approach. This approach is slightly more complex than discontinuous coupling, as some modification of the ocean state is required every coupling time step to account for changing ice topography, instead of restarting the ocean model each time from arbitrary initial conditions. The computational expense is basically the same as running uncoupled ocean and ice models. This is more expensive than discontinuous coupling, due to the need to continuously run the ocean model for the entire ice simulation. Moving from one fixed ice-shelf topography to another at the coupling step leads to continuity issues with mass, heat, salt, and momentum in the ocean that have to be solved with ad hoc techniques. This could lead to problems when using GCMs to consider sea level rise (mass) and warming (heat), as well as barotropic and baroclinic adjustments leading to “tsunamis” throughout the model domain (large spikes in velocity). The melt rate used in the ice model can lack detail both spatially and temporally as it is applied over an entire coupled time step rather than evolving along with ocean conditions, as well as potentially being spatially interpolated from the ocean grid to the ice grid. Examples of models using this approach currently being developed are given by Asay-Davis et al. (2016) and Seroussi et al. (2017).

The final approach, described in this manuscript, is that of “synchronous” coupling. In this approach, the ocean and ice models are both continuously run, with the coupled time step being the same as the ocean time step rather than of the order of the ice time step as in the previous two approaches. From a practical point of view, this is more difficult to achieve, as the ocean model code needs to be able to change ice-shelf geometry every time step, as well as properly interface with the ice-shelf code within a simulation. This approach can also be more expensive than asynchronous coupling as the ice model is being solved every ocean time step, and needs to share the ocean grid. However, this approach is fully conservative of heat, salt, and mass, which makes it well suited to problems with rapidly varying forcing. Synchronous

coupling is well suited to problems where the ocean model is not spun-up with respect to the ice model, a situation that would be impractical for a discontinuous model. If both the ocean and ice are varying rapidly then a discontinuous model may find its ocean spin-up time being of a comparable or greater length than its coupled time step, which is not an issue for the synchronous approach as there is no need to repeatedly spin-up the ocean. For example, tidal variation has been shown to affect the flow speed of ice streams (Gudmundsson, 2006). Strictly, this would require the ice model to represent viscoelastic flexural stresses, and it does not currently. However, from the oceanic side, our method of synchronous coupling can allow for large tidal deflections on a fast time scale, and implementing nonhydrostatic ice-shelf stresses is an area of active research. Additionally, the fast drainage of Antarctic subglacial lakes into ice-shelf cavities has been observed to have an impact upon melt rates, and possibly geometry change of the ice shelf (Smith et al., 2017), and is another process where both the ice and ocean are evolving rapidly, needing a synchronously coupled model to best resolve them. The model described in this manuscript is the first ice-ocean model to use this approach.

### 3. Coupled Model

Throughout this work, we use the MITgcm (Massachusetts Institute of Technology general circulation model) to model the complete ice-ocean system by coupling an ocean model (that can represent ice shelves) to an ice stream/shelf model. Both models being contained within the MITgcm framework vastly simplifies achieving a fully conservative coupling process, enabling a synchronously coupled ice-ocean model within one executable code. Note we only test this model in an ice shelf-ocean context; the implementation of a moving grounding line and grounded ice is discussed in a paper in preparation. A list of variables, their symbols and given values used throughout this manuscript can be found in Table 1.

Before going into detail about the individual parts of the model our approach to synchronous coupling can be summarized conceptually as follows. Melt rates from the ocean model viewed as vertical mass fluxes of freshwater are used to change the ice-shelf thickness in the ice model at every ocean time step. The thinning ice shelf leads to a reduced pressure load on the ocean from the ice shelf, which in turn leads to an inflow of ocean from surrounding cells. This results in a reduced ice-shelf draft. The changing shape of the ice-shelf draft will affect ocean dynamics and the resulting melt rate, bringing us full circle.

#### 3.1. Ocean Model

##### 3.1.1. Existing Model

The ocean is simulated using the MITgcm (Marshall et al., 1997), a  $z$  level coordinate model. The model utilizes the partial-cell functionality for topography (Adcroft et al., 1997) combined with a nonlinear ocean free surface that can change the partial-cell thickness in time (Campin et al., 2004). This allows more accuracy than a fixed  $\Delta z$  when representing both ocean floor bathymetry and ice-shelf basal topography. When using partial cells it is useful to define the open-cell fraction:

$$h_c = \frac{R}{\Delta z}, \quad (1)$$

where  $R$  is the vertical size of the cell and  $\Delta z$  is the vertical grid spacing (note that throughout this work we assume a constant  $\Delta z$ , the model does not require it). The fraction  $h_c$  is therefore usually 1, except potentially in the topmost and bottommost cells. The fraction  $h_c$  changes temporally in line with the ocean free surface and can become both greater than or less than 1 (Campin et al., 2004).

The ice-shelf forcing on the ocean is implemented using a method akin to that of Losch (2008). The vertical position of the ice-ocean interface,  $z_{surf}$  is defined relative to a reference ice-shelf basal depth,  $d$ , which itself is defined to adhere strictly to vertical grid boundaries (see section 3.1.3). When  $h_c$  in the topmost cell is equal to 1 this means  $z_{surf}$  is located at the topmost cell boundary. The position of the ice-ocean interface relative to the reference depth is defined as  $\eta$ . These relations are shown in Figure 1a and allow us to express the vertical position of the ice-ocean interface as:

$$z_{surf} = d + \eta. \quad (2)$$

##### 3.1.2. Thermodynamics

The ice-shelf melt rate is calculated using the three-equation formulation (Jenkins et al., 2010) with constant nondimensional heat and salt transfer coefficients ( $\Gamma_T$  and  $\Gamma_S$ , respectively). The rate formation is given by:

**Table 1**  
Model Variables and Parameters

Parameter	Symbol	Units	Value
Liquidus slope	$a$	$^{\circ}\text{C}$	0.0573
Velocity boundary layer thickness	$B_v$	m	20
Tracer boundary layer thickness	$B_k$	m	20
Liquidus intercept	$b$	$^{\circ}\text{C}$	0.0832
Liquidus pressure coefficient	$c$	$^{\circ}\text{C Pa}^{-1}$	$7.61 \times 10^{-4}$
Ice-shelf drag coefficient	$C_d$	n/a	0.0097
Specific heat capacity of ice	$c_i$	$\text{J}^{\circ}\text{C}^{-1} \text{kg}^{-1}$	2,009
Specific heat capacity of seawater	$c_{sw}$	$\text{J}^{\circ}\text{C}^{-1} \text{kg}^{-1}$	3,974
Reference ice-shelf depth	$d$	m	
Remesh check interval	$dt_{\text{remesh}}$	s	43,200
Salt flux	$F_S$	$\text{psu kg m}^{-2} \text{s}^{-1}$	
Heat flux	$F_T$	$\text{W m}^{-2}$	
Volume flux	$F_W$	$\text{m s}^{-1}$	
Acceleration due to gravity	$g$	$\text{m s}^{-2}$	9.81
Ice-shelf thickness	$H$	m	
Minimum ice-shelf thickness	$H_{\text{min}}$	m	0.05
Dimensionless vertical grid size	$h_c$	n/a	
Maximum dimensionless vertical grid size	$h_{\text{max}}$	n/a	1.3
Minimum dimensionless vertical grid size	$h_{\text{min}}$	n/a	0.29
Latent heat of ice fusion	$L$	$\text{J kg}^{-1}$	$3.34 \times 10^5$
Ablation rate of ice	$m$	$\text{m s}^{-1}$	
Pressure	$p$	Pa	
Surface mass balance	$q$	$\text{m s}^{-1}$	0
Vertical size of cell	$R$	m	
Salinity	$S$	psu	
Salinity at ice-ocean interface	$S_b$	psu	
Salinity of ice	$S_i$	psu	0
Surface salinity	$S_{\text{surf}}$	psu	0
Surface elevation	$s$	m	
Temperature	$T$	$^{\circ}\text{C}$	
Temperature at ice-ocean interface	$T_b$	$^{\circ}\text{C}$	
Depth-dependent freezing temperature	$T_f$	$^{\circ}\text{C}$	
Surface temperature	$T_{\text{surf}}$	$^{\circ}\text{C}$	
Temperature gradient of ice at ice-ocean interface	$\frac{\partial T_i}{\partial z} _b$	$^{\circ}\text{C m}^{-1}$	
U component of boundary layer velocity	$U_{\text{top}}$	$\text{m s}^{-1}$	
U component of ice velocity	$u_i$	$\text{m s}^{-1}$	
Friction velocity	$u_*$	$\text{m s}^{-1}$	
V component of boundary layer velocity	$V_{\text{top}}$	$\text{m s}^{-1}$	
V component of ice velocity	$v_i$	$\text{m s}^{-1}$	
Position of the calving front on the y axis	$Y$	m	60,000
Vertical position of the ocean free surface	$z_{\text{surf}}$	m	
Turbulent heat transfer coefficient	$\Gamma_T$	n/a	0.0135
Turbulent salt transfer coefficient	$\Gamma_S$	n/a	$2.65 \times 10^{-4}$
Vertical grid spacing	$\Delta z$	M	20
Two-dimensional strain rate tensor	Check : $\dot{\epsilon}$	$\text{s}^{-1}$	
Distance of ocean free surface from reference	$\eta$	m	
Thermal diffusivity of ice	$\kappa_i$	$\text{m}^2 \text{s}^{-1}$	$0.11 \times 10^{-6}$
Strain rate-dependent ice viscosity	$\mu_i$	Pa s	
Density	$\rho$	$\text{kg m}^{-3}$	
Ice density	$\rho_i$	$\text{kg m}^{-3}$	920
Reference density	$\rho_{\text{ref}}$	$\text{kg m}^{-3}$	1,000
Freshwater density	$\rho_{\text{fw}}$	$\text{kg m}^{-3}$	1,000
Seawater density	$\rho_{\text{sw}}$	$\text{kg m}^{-3}$	1,030
Backstress	$\Sigma$	N	
Average ice-shelf backstress	$\Sigma_{\text{avg}}$	N	
Geopotential	$\phi$	$\text{Pa kg}^{-1} \text{m}^3$	
Perturbation to the geopotential	$\phi'$	$\text{Pa kg}^{-1} \text{m}^3$	
Reference geopotential	$\phi_{\text{ref}}$	$\text{Pa kg}^{-1} \text{m}^3$	
Geopotential at reference ice-shelf depth	$\phi_d$	$\text{Pa kg}^{-1} \text{m}^3$	
Perturbation to the geopotential at reference ice-shelf depth	$\phi'_d$	$\text{Pa kg}^{-1} \text{m}^3$	

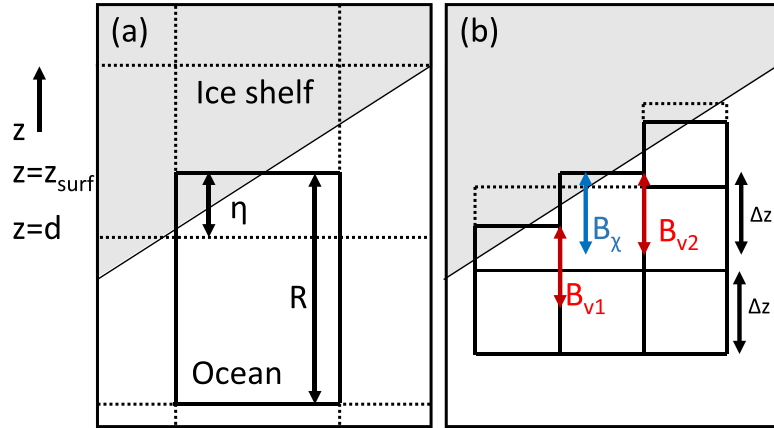


**Figure 1.** Schematic representation of (a) reference ice-shelf depth,  $d$ , vertical position of the ice-ocean interface,  $z_{surf}$ , and the distance between the two,  $\eta$ , and (b) the extent of the ice-shelf boundary layer used to calculate velocities,  $B_v$  (red), and tracers,  $B_{\chi}$  (blue), used in the melt rate calculation. The model grid is represented by dashed lines with the actual size of the cells represented by the solid lines.

$$m\rho_i L = \rho_i c_i \kappa_i \left. \frac{\partial T_i}{\partial z} \right|_b - \rho_{sw} c_{sw} u_* \Gamma_T (T_b - T) \quad (3)$$

$$T_b = aS_b + b + cz \quad (4)$$

$$m\rho_i (S_b - S_i) = -\rho_{sw} u_* \Gamma_S (S_b - S) \quad (5)$$

with  $m$  the ablation rate of ice (expressed as a mass change per unit time, positive for melting),  $\rho_i$  and  $\rho_{sw}$  the density of ice and seawater, respectively,  $L$  the latent heat of ice fusion,  $c_i$  and  $c_{sw}$  the specific heat capacity of ice and seawater, respectively,  $u_*$  the friction velocity,  $\kappa_i$  the thermal diffusivity of ice,  $\left. \frac{\partial T_i}{\partial z} \right|_b$  the ice temperature gradient at the ice-ocean boundary,  $T_b$  (assumed to be at the pressure-dependent freezing temperature) and  $S_b$  the temperature and salinity at the ice-ocean interface,  $T$  and  $S$  the “far-field” ocean temperature and salinity in the boundary layer,  $a$ ,  $b$ , and  $c$  are constants, and  $S_i$  is the salinity of ice.

This leads to a flux of heat ( $F_T$ ) and salt ( $F_S$ ) across the boundary, positive in the direction of the ice shelf (Jenkins et al., 2001), defined as:

$$F_T = -c_{sw} (\Gamma_T u_* \rho_{sw} (T_b - T) + m\rho_i (T_b - T_{surf})) \quad (6)$$

$$F_S = -(\Gamma_S u_* \rho_{sw} (S_b - S) + m\rho_i (S_b - S_{surf})) \quad (7)$$

with  $T_{surf}$  and  $S_{surf}$  the temperature and salinity of the model cell adjacent to the ice-ocean interface. Note that the first term on the right-hand side of (6) and (7) is the diffusive flux of heat and salt toward the ice and the second term is the advective meltwater flux to the ocean. This second term arises from the fact that the meltwater flow is not explicitly included in the ocean model (Jenkins et al., 2001). These salt and heat fluxes are applied using the boundary layer method of Losch (2008) in combination with an input of a “real” meltwater volume flux ( $F_W$ ) in a manner akin to that used to simulate evaporation and precipitation, making the melting process fully conservative of heat, salt, and mass. The volume flux input in this case is equivalent to the water released with an ablation rate of  $m$ , i.e.:

$$F_W = m \frac{\rho_i}{\rho_{fw}} \quad (8)$$

with  $\rho_{fw}$  the density of freshwater.

The ocean properties  $T$ ,  $S$ , and  $u_*$  used in this formulation are a weighted average of a boundary layer ( $B_{\chi}$  for tracer properties and  $B_v$  for velocities) over a distance of  $\Delta z$  from the ice-ocean interface (Figure 1b). Boundary layer tracer properties are therefore the same as the topmost cell when  $h_c \geq 1$  and a weighted average of the topmost two cells when  $h_c < 1$ . The formulation requires  $u_*$  to be defined at the same location as the tracer properties temperature and salinity. As MITgcm uses a c-grid, the vertically weighted

average over  $\Delta z$  of the four horizontally adjacent points on the velocity grid to the tracer point in question is used. This gives rise to a friction velocity  $u_*$  that is used in melt rate calculations, defined as:

$$u_*^2 = C_d (V_{top}^2 + U_{top}^2), \quad (9)$$

where  $C_d$  is the dimensionless ice-shelf drag coefficient and  $V_{top}$  and  $U_{top}$  are the average  $v$  and  $u$  velocities in the boundary layer, obtained by first calculating a weighted average of velocities a distance of  $\Delta z$  from the ice-ocean interface on the velocity grid, then horizontally interpolating these values onto the tracer grid and finally the combined  $u$  and  $v$  velocities are squared (then square rooted) to give  $u_*$ .

In contrast to the current version of MITgcm, we define the boundary layer velocity to be over  $\Delta z$  of water from the ice-ocean interface at the velocity points rather than the interface at the tracer points (Figure 1b). In practice, this results in the ocean velocity being relatively larger in our method compared to the previous implementation, and minimizing the impact of grid discretization. A  $z$  level model, such as the MITgcm, tends to give “stripy” melt rates of alternating high and low melt rates when  $d$  differs between two neighboring cells in the horizontal plane. This leads to the cells being at different  $z$  levels and having a reduced  $u_*$  due to the no-flow conditions at the velocity points on vertical ice-shelf faces. In the implementation of Losch (2008), the model grid was defined so that the topmost wet cells, if partial cells, had thickness less than  $\Delta z$ . In our implementation having cells larger than  $\Delta z$  is unavoidable, which initially led to a worsening of the “stripy” melt rate artifact seen in Losch (2008). Our method of calculating  $u_*$  acts to minimize this by ensuring that no “zero flow” walls are averaged into  $u_*$ . Furthermore, the model remeshing described below (section 3.1.4) has the added benefit of evolving the discretization during the simulation, reducing the impact of this problem at any given location.

### 3.1.3. Pressure

The momentum solver in MITgcm does not use pressure  $p$  directly, but rather pressure-potential which is simply defined as  $\phi = \frac{p}{\rho_{ref}}$  in the Boussinesq framework. Additionally the baroclinic pressure gradient is found directly from the perturbation to the geopotential,

$$\phi' = \phi - \phi_{ref} = \phi - \int_z^0 g dz \quad (10)$$

with  $g$  being the acceleration due to gravity. The perturbed geopotential at  $z$  can be written as:

$$\begin{aligned} \phi' &= \phi'_d + g(z_{surf} - d) + \int_z^{z_{surf}} g \frac{\rho - \rho_{ref}}{\rho_{ref}} dz \\ &= \phi'_d + g\eta + \int_z^{z_{surf}} g \frac{\rho - \rho_{ref}}{\rho_{ref}} dz, \end{aligned} \quad (11)$$

where the first term is due to the load placed at the reference surface  $d$  (or rather, the load minus the background potential); the second is due to the variation of the free surface  $z_{surf}$  from the reference surface, and the third is the vertical integral of buoyancy leading to the baroclinic pressure. Note that the integral in the third term has upper bound  $z_{surf}$  rather than  $d$  and no approximation of buoyancy is used over the interval  $[d, z_{surf}]$ . This is due to our use of the nonlinear free surface capability of the ocean model (Campin et al., 2004). In this implementation, the free surface  $\eta$  adjusts each time step as part of the barotropic mass and momentum stepping. The work of Losch (2008) generalized this formulation to allow  $d$  to be located at the base of the ice shelf rather than at sea level. In our coupling implementation,  $\phi'_d$  is the geopotential perturbation associated with the ice overburden:

$$\phi'_d = g \left( \frac{\rho_i H}{\rho_{ref}} - d \right), \quad (12)$$

where  $\rho_i H$  is the ice-shelf mass per unit area, with  $H$  being the ice thickness. This allows changes in ice thickness to be translated to changes in surface pressure at each ocean time step, therefore permitting a coupled time step that is the same as the ocean time step.

Note this approach is distinct from the approach of Losch (2008) which does not explicitly specify ice mass, but rather specifies  $d$  as the “target” ice draft and defines  $\phi'_d$  such that  $\eta = 0$  (and thus the ocean surface is at  $d$ ) when the ocean is quiescent with the initial density profile. Our approach also differs from Losch (2008) in that  $d$  now is at the same depth as vertical grid boundaries, yielding values of  $\eta$  that are potentially

large even when the ocean is stagnant. This is not an issue, however, as it can be seen from (11) and (12) that the geopotential is invariant to a redefinition of  $d$ , as long as  $\eta$  is similarly redefined to keep  $z_{surf}$  unchanged.

In order to avoid cell thicknesses that are too large (increasing discretization error), or are negative,  $d$  will eventually need to be modified (described later in section 3.1.4). Changing  $d$  every time step in response to changing ice-shelf mass, however, is costly as it would require a redefinition of the linear system that is solved for the free surface update (Campin et al., 2004). A compromise, then, is to only change  $d$  when remeshing occurs, which necessarily means that  $\eta$  will undergo variations of order  $\Delta z$ . We choose to align  $d$  with vertical cell faces for ease of development. Specifically,  $d$  is always located at the topmost ocean cells upper vertical grid boundary.

### 3.1.4. Remeshing

We have developed the MITgcm such that the evolving ice sheet model and ice-shelf melting changes the ocean domain, with the ocean mesh evolving accordingly. The use of partial cells leads to top cells with varying  $h_c$  in both time and space, with problems arising for too large or small an  $h_c$ . Too large an  $h_c$  leads to a poor representation of the boundary layer required for calculating the melt rate, while too small an  $h_c$  can lead to unrealistically high velocities. If either occurs it is necessary to update the model grid. Upon initialization of MITgcm, ocean model grid cells are flagged as being either ice or ocean. The remeshing process described here essentially allows ocean model cells to switch from ice to ocean, and vice versa, within a model run and without the need to reinitialize initial ice and ocean masks. While  $h_c$  continuously evolves every time step, at a predetermined interval ( $dt_{remesh}$ ) we check to see if it has grown above  $h_{max}$  or below  $h_{min}$ . If it has then we trigger the remesh process, essentially redefining  $d$ , the reference depth of the ice shelf that the position of the ocean free surface ( $z_{surf}$ , located at the ice-ocean interface under an ice shelf) is relative to.

This is done by either splitting a cell with too large an  $h_c$  into two smaller cells or merging a cell with too small an  $h_c$  with another cell to create a single large cell. This process is shown in Figure 2. Figure 2a shows the top layer of partial cells under an ice shelf. As the ice-shelf thickness decreases, the position of the ice-ocean interface is raised. This leads to cell  $i = 2, k = 2$  to have a larger  $h_c$  than  $h_{max}$  (Figure 2b). The cell is then split into two new cells, positioned at  $i = 2, k = 2$  and  $i = 2, k = 1$ , respectively (Figure 2c). Similarly, when merging a cell with  $h_c$  less than  $h_{min}$  with the cell below, the process happens in reverse. If cell  $i = 2, k = 1$  in Figure 2c were too small it would need to be merged with  $i = 2, k = 2$ . The resultant cell,  $i = 2, k = 2$  in Figure 2b, would have the combined  $h_c$  of cells  $i = 2, k = 1$  and  $i = 2, k = 2$  from Figure 2c.

When a cell is split into new cells all tracer properties are conserved, with the two new cells taking the properties of the old cell.

$$\chi^{old} = \chi^{lower} = \chi^{upper}, \tag{13}$$

where  $\chi^{old}$  is a tracer property of the old cell being split into upper and lower cells with tracer properties  $\chi^{lower}$  and  $\chi^{upper}$  respectively. The same relationship holds for velocities on all faces, however when new cell creation leads to a new solid ice boundary (as in Figure 2) then the velocity on this boundary is set to zero. The  $h_c$  of the two new cells are given by:

$$h_c^{old} = h_c^{lower} + h_c^{upper} = 1 + (h_c^{old} - 1), \tag{14}$$

where  $h_c^{old}$ ,  $h_c^{lower}$  (equal to 1 in this case), and  $h_c^{upper}$  the dimensionless size of the old, large cell and two new cells, respectively. As there has been a change in the cells masked as ice or ocean we also need to update the reference position of the ice shelf,  $d$ , such that

$$d^{new} = d^{old} + \Delta z, \tag{15}$$

where  $d^{old}$  is the old reference depth of the ice shelf and  $d^{new}$  is the new reference position. During this process, the vertical position of the ocean free surface never changes, such that in the topmost ocean cell:

$$z_{surf}^{new} = d^{new} + \eta^{new} = d^{old} + \eta^{old} = z_{surf}^{old}, \tag{16}$$

where  $z_{surf}^{old}$ ,  $z_{surf}^{new}$  and  $\eta^{old}$ ,  $\eta^{new}$  are the old and new positions of the ice-ocean interface and its distance from the reference depth of the ice shelf, respectively.

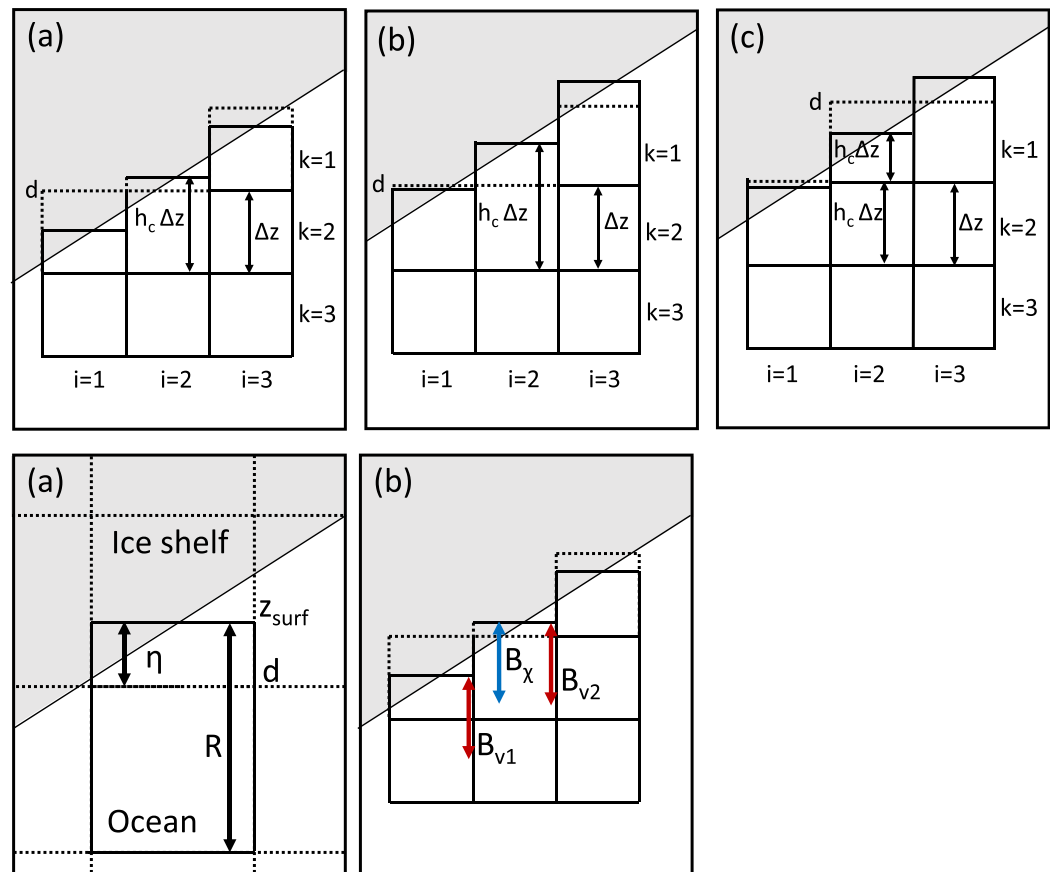


**Figure 2.** Schematic representation of dimensionless vertical grid size,  $h_c$ , and reference ice-shelf depth,  $d$ , at  $i = 2$  in (a) a “normal” case, (b) a cell with  $h_c > h_{\max}$  at  $i = 2, k = 2$  just before a model remesh check, and (c) the same cell just after a model remesh has occurred. The model grid is represented by dashed lines, the actual size of model cells by solid lines.

When merging two cells with  $h_c^{\text{lower}} (=1)$ ,  $\chi^{\text{lower}}$  and  $h_c^{\text{upper}}$ ,  $\chi^{\text{upper}}$ , respectively, then (14) and (15) still apply, only in reverse, but (13) becomes:

$$\frac{\chi^{\text{lower}} h_c^{\text{lower}} + \chi^{\text{upper}} h_c^{\text{upper}}}{h_c^{\text{new}}} = \chi^{\text{new}} \quad (17)$$

which also holds for velocities on cell faces.

### 3.2. Ice Stream Model

Taking advantage of MITgcm’s parallel computing and adjoint modeling support framework, the code has in recent years been extended to enable coupled ice shelf-ice stream simulations. The corresponding “streamice” package of the MITgcm uses a hybrid stress balance, defaulting to the two-dimensional shallow shelf approximation (MacAyeal, 1989) equations when no grounded ice is present, and described in greater detail in Goldberg and Heimbach (2013). The shallow shelf approximation (SSA) consists of the momentum balance for vertically integrated horizontal velocity:

$$\partial_x [H\mu_i(4\dot{\epsilon}_{xx} + 2\dot{\epsilon}_{yy})] + \partial_y [2H\mu_i\dot{\epsilon}_{xy}] = \rho_i g H s_x, \quad (18)$$

$$\partial_x [2H\mu_i\dot{\epsilon}_{xy}] + \partial_y [H\mu_i(4\dot{\epsilon}_{yy} + 2\dot{\epsilon}_{xx})] = \rho_i g H s_y, \quad (19)$$

where  $u_i$  and  $v_i$  are the ice velocity,  $\dot{\epsilon}(u_i)$  is the two-dimensional strain rate tensor,  $s$  is surface elevation, and  $\mu_i(\dot{\epsilon})$  is the strain rate-dependent viscosity. Boundary conditions must be given at the surface and the lateral boundaries. The surface (defined by  $z = s(x, y)$ ) and base (always floating in our domain) are assumed to be stress-free, and the lateral boundary conditions

$$\mu_i [\vec{n}_x (4u_{ix} + 2v_{iy}) + \vec{n}_y (v_{ix} + u_{iy})] = \frac{1}{2} \rho_i g \left( 1 - \left( \frac{\rho_i}{\rho_{sw}} \right) \right) H \vec{n}_x, \quad (20)$$

$$\mu_i [\vec{n}_x (v_{ix} + u_{iy}) + \vec{n}_y (4v_{iy} + 2u_{ix})] = \frac{1}{2} \rho_i g \left( 1 - \left( \frac{\rho_i}{\rho_{sw}} \right) \right) H \vec{n}_y, \quad (21)$$

hold, where  $\vec{n}$  is the unit normal to the surface. Thickness evolves according to the continuity equation:

$$\frac{\partial H}{\partial t} + \nabla \cdot (H \vec{u}_i) = q - m \quad (22)$$

with  $q$  the surface mass balance and  $m$  is, again, the ice ablation rate (positive when melting). In its current implementation, the model cannot handle floating regions that are disconnected from the calving front or any lateral boundaries, i.e., large icebergs. As such we impose a minimum value of ice thickness ( $H_{min}$ ), typically of a few centimeters. It is assumed that ice that has reached this thickness has completely melted away.

In this study, the ice domain consists of the ice shelf only, with an imposed inflow velocity. In the experiments below, we examine the stress state and diagnose the total buttressing, i.e., the integrated shear stress along the ice-shelf sidewalls ( $\Sigma$ ), given by:

$$\Sigma = \vec{n}_x \int_0^Y \mu_i H \left( \frac{\partial v_i}{\partial x} + \frac{\partial u_i}{\partial y} \right) dy \quad (23)$$

with  $\vec{n}_x$  being the unit vector inward normal to the wall and  $Y$  being the position of the calving front on the  $y$  axis. The shelf average back stress,  $\Sigma_{avg}$ , is simply the average of  $\Sigma$  evaluated at both of the ice-shelf lateral margins. By diagnosing the shear stress in this way, we neglect potentially important feedbacks such as changes in inflow velocity and lengthening of the ice shelf further due to grounding line retreat (along with potential further changes to inflow speed due to variable topography). In this sense our study looks at the early response in buttressing to coupled ice shelf-ocean evolution. The synchronous coupled model is currently being further developed to allow grounded ice and a moving grounding line.

The interface between ice and ocean involves passing the ice thickness  $H$  to the ocean code which calculates  $\phi'_{di}$ , and using the melt rate calculated by the ocean model to update the ice-shelf mass balance (22). Using an inbuilt ice sheet code makes it easy to do this on a per-ocean time step basis. Solving (18) and (19) in each ocean time step would be prohibitively expensive; this is because the system of PDEs is nonlocal and nonlinear (with the viscosity dependent upon the velocity field), and is solved through an iterative procedure, with each iteration requiring the solution of a large linear system. On the other hand, the change in velocity associated with thickness change over an ocean time step is negligible. In our time stepping strategy, (22) is implemented each ocean time step with the latest ocean melt rate. A single iteration of the solver for (18) and (19) is computed every ice time step (typical on the order of 12 h) to update ice velocities and it is assumed that thickness change over this period is sufficiently small that only a single iteration is required. A similar "split time step" strategy was used by Walker and Holland (2007). With this time stepping strategy, the ice model comprises  $\sim 1$ – $2\%$  of the total coupled model run time. Therefore, the cost of the coupled model is essentially the same as that of the ocean model alone.

#### 4. Experimental Design

The ocean model mesh is 160 by 60 cells in the horizontal with a 1 km grid resolution and 55 cells in the vertical with a constant  $\Delta z$  of 20 m grid resolution. No-slip boundary conditions are applied to ocean velocities at the east, west, and south as well as the ocean floor and ice-ocean interface, while no-slip boundary conditions are applied to the ice at the east and west. Temperature and salinity are restored to initial conditions at the northern boundary in a five cell wide linear sponge layer over a time period of one day. To account for the changing ocean volume within the domain due to the (neglected) change in the flux of ice across the calving front, the average open-ocean sea-surface height (SSH) is restored to zero through adjustment of the open boundary barotropic velocity. That is, if there is a net mass loss in the closed ice/ocean domain, to prevent continually sinking SSH, there will be a small net inflow of water across the northern boundary, restored to the prescribed temperature and salinity, which ensures the open-ocean SSH is

always maintained to a zero average. Horizontal diffusivity and viscosity are both set to a constant  $100 \text{ m}^2 \text{ s}^{-1}$ , while vertical diffusivity and viscosity are  $1 \times 10^{-3} \text{ m}^2 \text{ s}^{-1}$  and  $5 \times 10^{-5} \text{ m}^2 \text{ s}^{-1}$ , respectively. An ocean time step of 60 s has been used throughout, except for the first month of the “Warm” simulation (see below), where a time step of 30 s was required to prevent a failure of the model to converge. Rotation is accounted for by means of an  $f$  plane at the equivalent of  $70^\circ\text{S}$ .

Initial temperature and salinity profiles for the baseline case have warm, salty water ( $1.2^\circ\text{C}$ , 34.7 psu) at depth and cold, freshwater at the surface ( $-1^\circ\text{C}$ , 34 psu). These two water masses are separated by a linearly varying pycnocline of 400 m thickness, starting at 300 m depth. These temperature and salinity profiles are consistent with previous work on Pine Island Glacier (PIG) (De Rydt et al., 2014). Sensitivity studies have been carried out around this baseline by varying the depth of the pycnocline by  $\pm 100 \text{ m}$  and 200 m in both directions, but maintaining its thickness of 400 m. This gives us five different forcings, henceforth referred to by the depth of the upper limit of the pycnocline (100, 200, 300 (baseline), 400, 500). A “Warm” and “Cold” run were also carried out, with water conditions constant in depth (and hence no pycnocline) at the previously mentioned warm and cold water masses (Figure 3).

The ice-model mesh extends 60 km from the southern boundary, sharing a grid with the 1 km horizontal resolution ocean mesh. The initial ice-shelf geometry was generated by running the ice stream model on its own without any basal melting until steady state. A Glen’s law exponent of  $n = 3$  is used in combination with a Glen’s law coefficient of  $B = 4.9 \times 10^5 \text{ Pa a}^{-3}$  (corresponding to an ice temperature of roughly  $-15^\circ\text{C}$ ). Ice enters the domain with a constant flux, achieved by maintaining a fixed ice-shelf draft of 900 m at the southern boundary along with an inflow velocity that peaks at  $2 \text{ km a}^{-1}$  in the center of the domain and falls to  $0 \text{ km a}^{-1}$  at the margins. Ice that moves past the calving front located 60 km from the southern boundary is removed from the domain. Ice velocities within the domain are updated at the ice time step of 43,200 s, while ice thickness is updated every coupled time step which is the same as the ocean time step of 60 s.

Our test domain is designed to represent a typical warm-water ice shelf, such as PIG. The domain is 60 km wide and 160 km long, with a depth of 1100 m (Figure 4). The ice shelf has an initial extent of 60 km, beyond which it is not allowed to advance, although retreat is possible through thinning to the minimum ice-shelf thickness. The ice shelf flows into the domain through a boundary we refer to as “south,” and calves in the opposite direction which we refer to as “north.” The coupled model was run for a period of 60 years with monthly output, and all simulations had reached a steady state by the end of this period. As well as these coupled runs, ice only runs with parameterized melt rates (described more fully in section 5.4) were carried out for the same forcings. In all cases, we are interested in how the ice-shelf thickness evolves

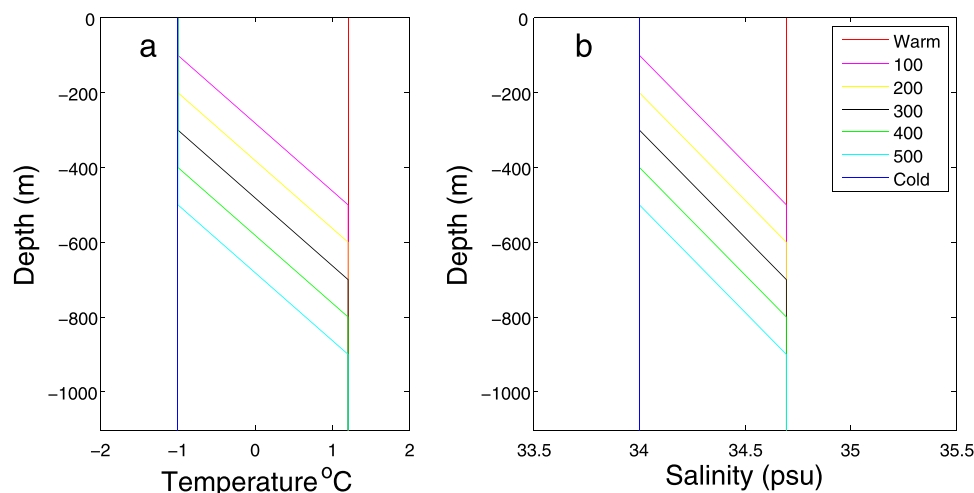


**Figure 3.** (a) Initial temperature and (b) salinity profiles for the seven forcings. Temperature and salinity are restored to these profiles at the northern boundary. The forcing labels refer to the depth of the start of the pycnocline which separates cold freshwater at the surface from warm salty water at depth. Two additional simulations use constant warm, salty water or cold, freshwater.

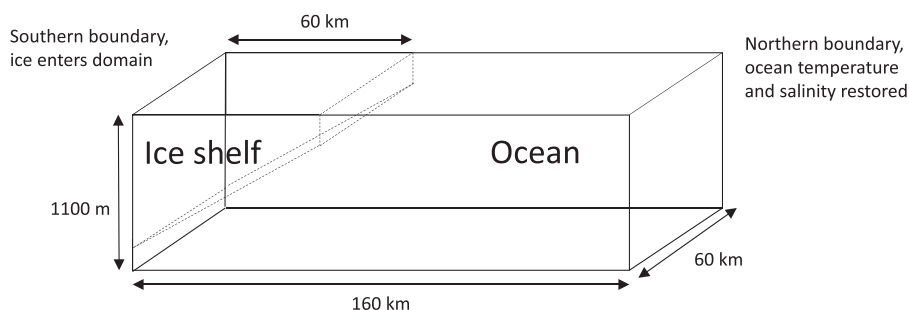


Figure 4. Schematic representation of model domain.

over time and its impact upon ice-shelf backstress (and therefore buttressing). Constants not explicitly defined have the values given in Table 1.

## 5. Results

### 5.1. Time Stepping Comparison

Before presenting results, we briefly compare the accuracy of our ice-model split time stepping with more traditional ice sheet time stepping. We carry out an ice only experiment with ice domain and model parameters as described above, where an initially steady ice shelf is forced by a constant melt rate of  $5 \text{ m a}^{-1}$  and allowed to evolve. We carry out one simulation with split time stepping, where thickness is updated every 60 s and velocity every 43,200 s without convergence. In addition we carry out two simulations in which the momentum balance is iterated to convergence, and the thickness is updated via continuity, on the same time step. Figure 5 shows the root mean square difference in thickness between the simulations. Over 50 years, the difference between split and 0.1 year time stepping grows to  $\sim 0.6 \text{ m}$ , which is small relative to the overall change in thickness (of order several hundred meters). Furthermore, the comparison with 0.025 year time stepping is only  $\sim 0.15 \text{ m}$ , implying a linear convergence of the long-time step simulations toward the split time step solution. As such the use of split time stepping does not significantly affect our results, while decreasing the cost of the simulations.

### 5.2. Baseline Simulation Time Evolution

In a fully coupled ice-shelf model the ice-shelf geometry affects the ocean flow, which in turn affects the melt rate, and thus the ice-shelf geometry. While we will discuss these effects separately it should be noted that they are all happening simultaneously, creating feedbacks with one another within the model. We first look at a representative (baseline 300 m pycnocline depth, typical of a warm-water ice shelf) run and examine in detail the processes occurring in the fully coupled evolution of ice-shelf geometry.

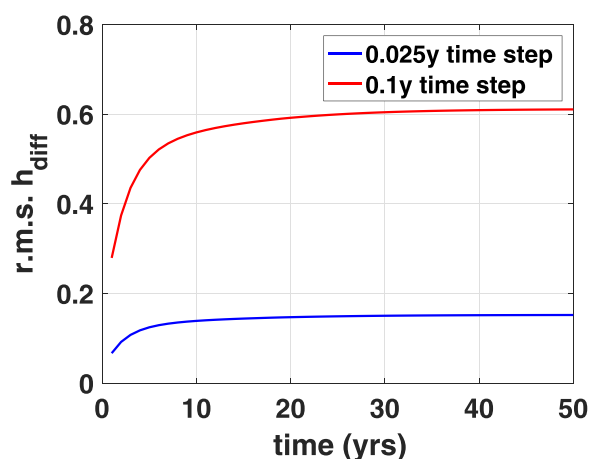
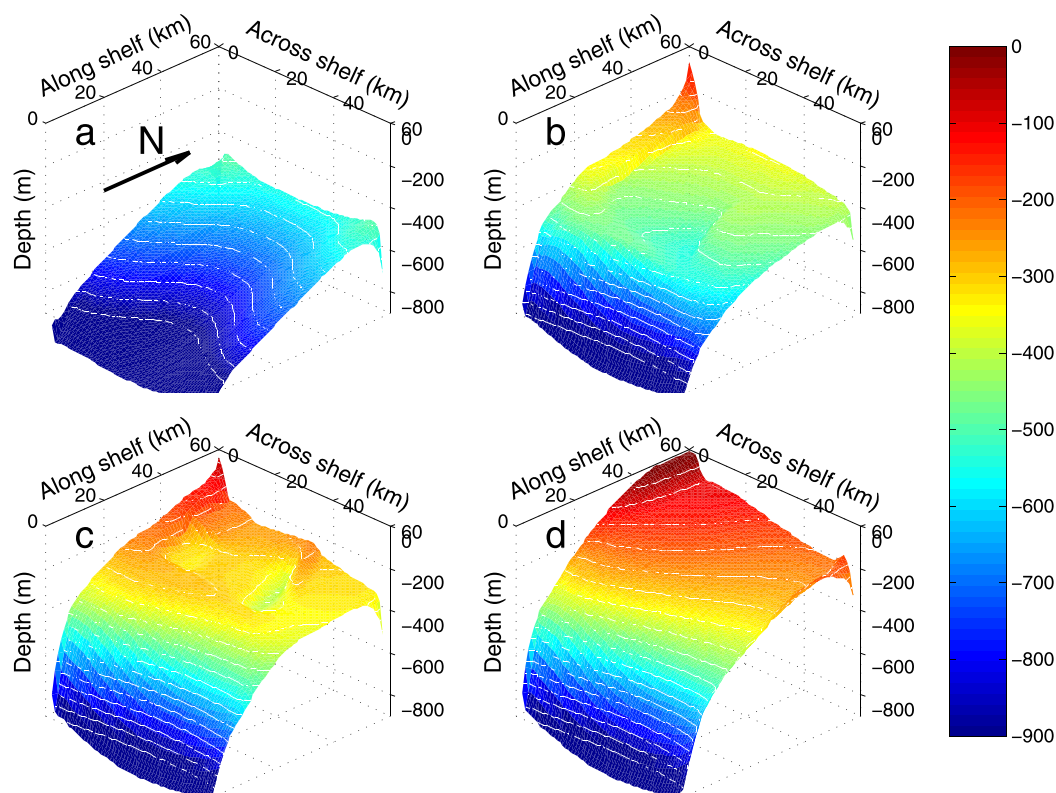


Figure 5. Comparison of the difference in ice-shelf thickness between using split ice-model time stepping or conventional time stepping.

This evolution of the ice-shelf thickness in the baseline run is shown in Figure 6. Initially, the ice is symmetrical about a central “bulge” (Figure 6a), with thicker ice being present in the middle of the domain when compared to the eastern and western boundaries. When melting is applied, however, this symmetry is quickly lost. Within 5 years the ice shelf has thinned noticeably, with a pronounced channel appearing along the western boundary (Figure 6b). After 13 years, the channel is still present, although its rate of formation is slowed (Figure 6c). There are also the remnants of the initial central “bulge,” which is advected toward the ice front by ice that has entered the domain since melting began. This transitory period has ended by the time 60 years has passed, and a new steady state has established itself (Figure 6d). This state is characterized by the presence of a western channel, although relative to the rest of the ice shelf not as deep when compared to the transitory phase. The central “bulge” that was present in the initial conditions has now been deflected to the east by preferential melting in the west, leading to the western half of the ice shelf being comparatively thinner than the eastern half.



**Figure 6.** Evolution of ice-shelf depth (colors, 50 m depth contours) for (a) initial, (b) year 5, (c) year 13, and (d) year 60 in the baseline 300 m pycnocline depth case.

This changing ice-shelf geometry influences the oceanic flow within the model domain (Figure 7). With the initial geometry, the flow is directed toward the western, Coriolis-favored side. The flow moves past the central “bulge” if possible and then flows almost due west until it hits the western boundary, creating a strong boundary current. While the majority of the flow leaves the ice-shelf cavity via the western channel, some flow leaves the domain on the eastern side of the “bulge.” After 5 years this boundary current has induced high melting, leading to a self-reinforcing channel at the western boundary. The central “bulge” is quickly melted away. After 13 years since the beginning of the simulation there is an overall reduction in boundary layer velocity over much of the shelf, except near the grounding line and the western channel. The remnants of the initial “bulge” still direct flow around it, although it is quickly being advected off the shelf to be replaced by thinner ice that melted nearer the grounding line. The final, steady state ocean flow maintains the pattern of greatest flow velocity at depth and in the western channel. There is now a “bulge” on the eastern side of the shelf rather than the center, with flow being restricted on its eastern side. It should be noted that the pronounced thickness in the north eastern corner of the ice shelf arises as a consequence of the no-slip boundary condition for ice joining up with the calving front in an area of low melting, leading to lateral spreading along the front and piling up of ice. The same is not true of the western boundary, as residual ice is removed via melting.

This ocean flow drives the melting of the ice shelf (Figure 8), which itself is dependent upon  $u_*$  and thermal driving ( $T - T_f$ , where  $T_f$  is the pressure-dependent freezing point). Initial conditions show highest melting on the western boundary, as well as western side of the “bulge.” There are also relatively high melt rates over much of the ice shelf. These melt rates are primarily driven by the high initial thermal driving all across the ice shelf due to initializing the ice geometry from a nonmelting case, with a correspondingly thicker ice shelf protruding into warmer waters. The only part of the ice shelf with low thermal driving is the western channel. As the initial geometry is symmetrical, the low thermal driving is a result of the water in the western channel being composed of predominantly meltwater which is fresher and colder than the surrounding water. The fact the meltwater plume in the western channel is less dense than the surrounding water

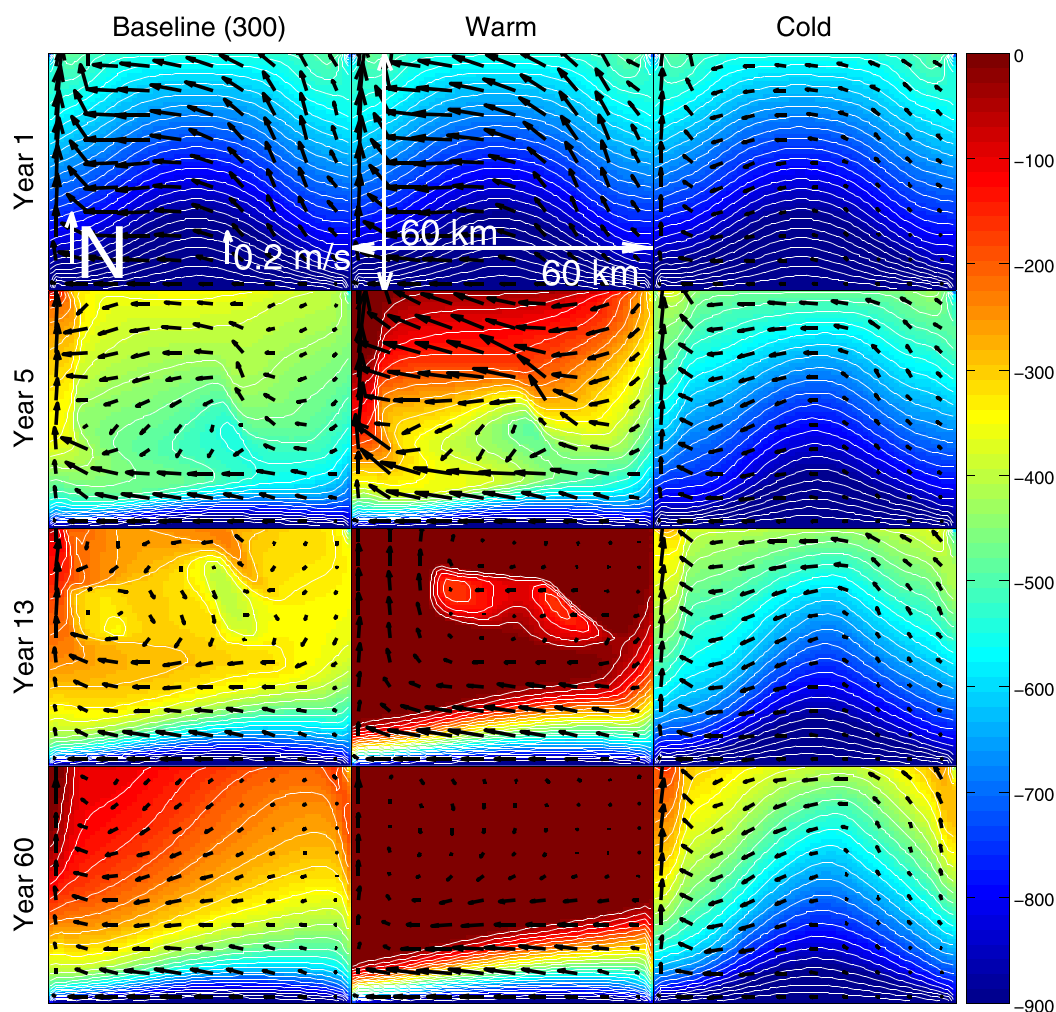


**Figure 7.** Ice-shelf depth (colors, 50 m contours) with ice-shelf boundary layer velocities (arrows) for the baseline 300 m pycnocline depth, warm and cold forcings at year 1, year 5, year 13, and year 60.

contributes to the high  $u_*$  observed here, greater than anywhere else in the domain. After 5 years melt rates have fallen dramatically. High melt rates remain at the grounding line, where new ice is entering the domain at depth, where thermal driving is greatest.

Melt rates are low over much of the ice shelf, except in the western channel. The low melt rates on the shelf as a whole are a result of low thermal driving and  $u_*$ , though the central “bulge” is generating high thermal driving when present. The relatively high melt rates in the western channel are due to the relatively high  $u_*$  present, as there is still very low thermal driving here due to the meltwater plume. After 13 years, the vast majority of ice-shelf melting is happening near the grounding line, with very little melt elsewhere, including the western channel. This is despite there being the highest values of  $u_*$  in the western channel. The final, steady state after 60 years is similar, with melting predominantly happening at the grounding line due to the combination of high thermal driving and  $u_*$ . The western channel now acts to channel the release of meltwater from the ice shelf, with melt rates limited by the low thermal driving of meltwater despite a high  $u_*$  from the western boundary flow.

### 5.3. Coupled Temperature Variation Runs

As well as the baseline case described previously (300 m pycnocline depth), Figure 6 also shows the time evolution of the ice-shelf depth and boundary layer flow for the warm and cold cases’ (videos of the evolution of ice-shelf thickness and melt rate for these three cases can be found in the supporting information).

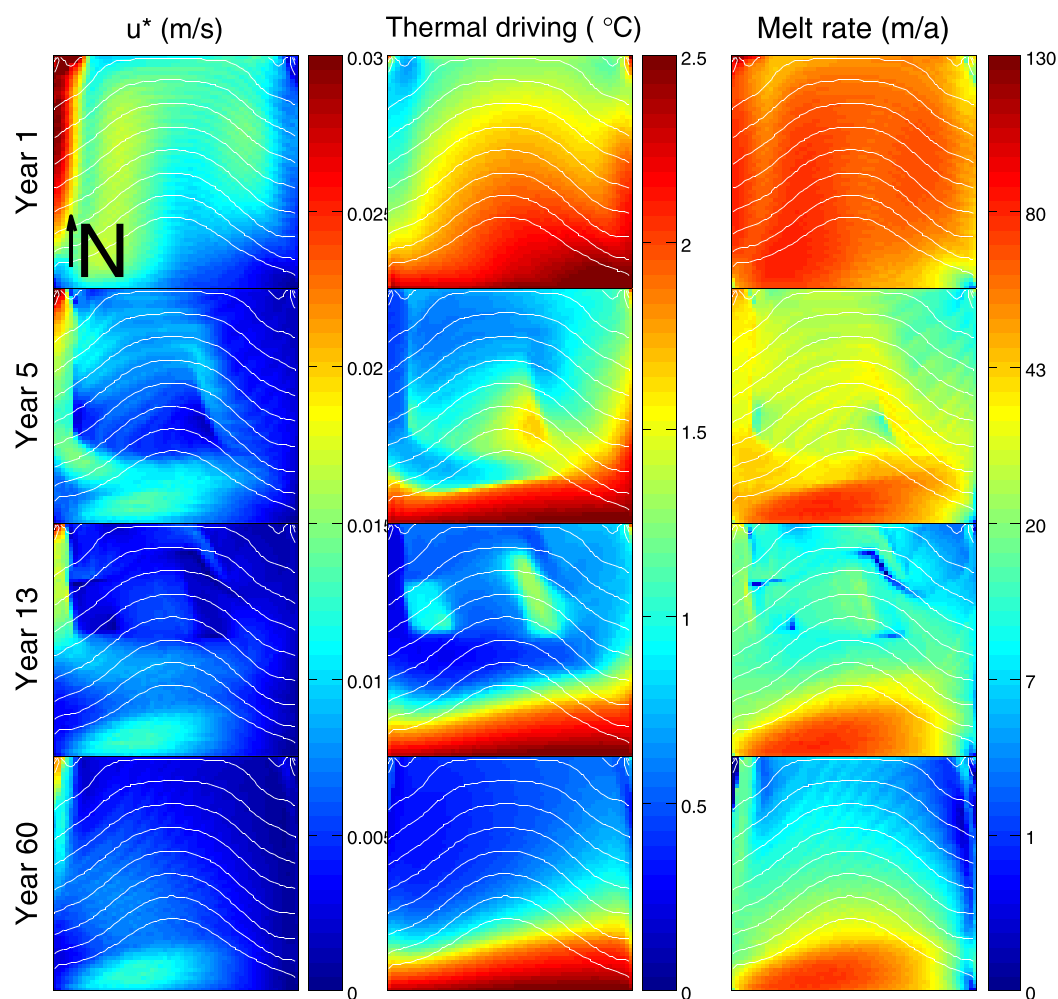


**Figure 8.** Ice-shelf depth (50 m contours) with melt rate, thermal driving and  $u_*$  for the baseline 300 m start of pycnocline depth forcing at years 1, 5, 13, and 60.

The warm case starts from the same initial conditions as the baseline case, however due to the increased thermal driving throughout the water column it melts at an increased rate. By 5 years, there is not only a pronounced western channel, but the ice shelf has melted to its minimum thickness in places. Ocean flow is still favoring the western side due to Coriolis forcing, with the remains of the initial “bulge” directing flow around it. After 13 years, the vast majority of the ice shelf has melted to its minimum thickness, with the last remnants of the initial “bulge” detaching from the remains of the ice shelf as a pseudoiceberg and subsequently exiting the domain. The steady state for the “warm” case has an ice shelf resembling a triangular wedge, slightly thinner on the Coriolis-favored western side.

In contrast, the cold case does not change greatly from its initial conditions. While the imposition of melting causes a slight overall reduction in ice-shelf thickness the general shape of the ice shelf, including the central “bulge,” remains largely intact. There is a small change in ice-shelf thickness at the western boundary, but much smaller than in the baseline case. Ocean flow is still affected by the presence of the “bulge,” needing to find its way around it as it heads to the western, Coriolis-favored side.

The final steady state ice-shelf geometry for the seven forcings is shown in Figure 9. Increased ice-shelf melt (due to a raising of the pycnocline) tends to progressively thin the western boundary, with the highest melting forcings (Figures 9a–9c) resembling a triangular wedge. The lowest melting forcings (Figures 9e–9g) in contrast maintain a “bulge” toward the center despite the presence of a melt-driven western boundary channel.

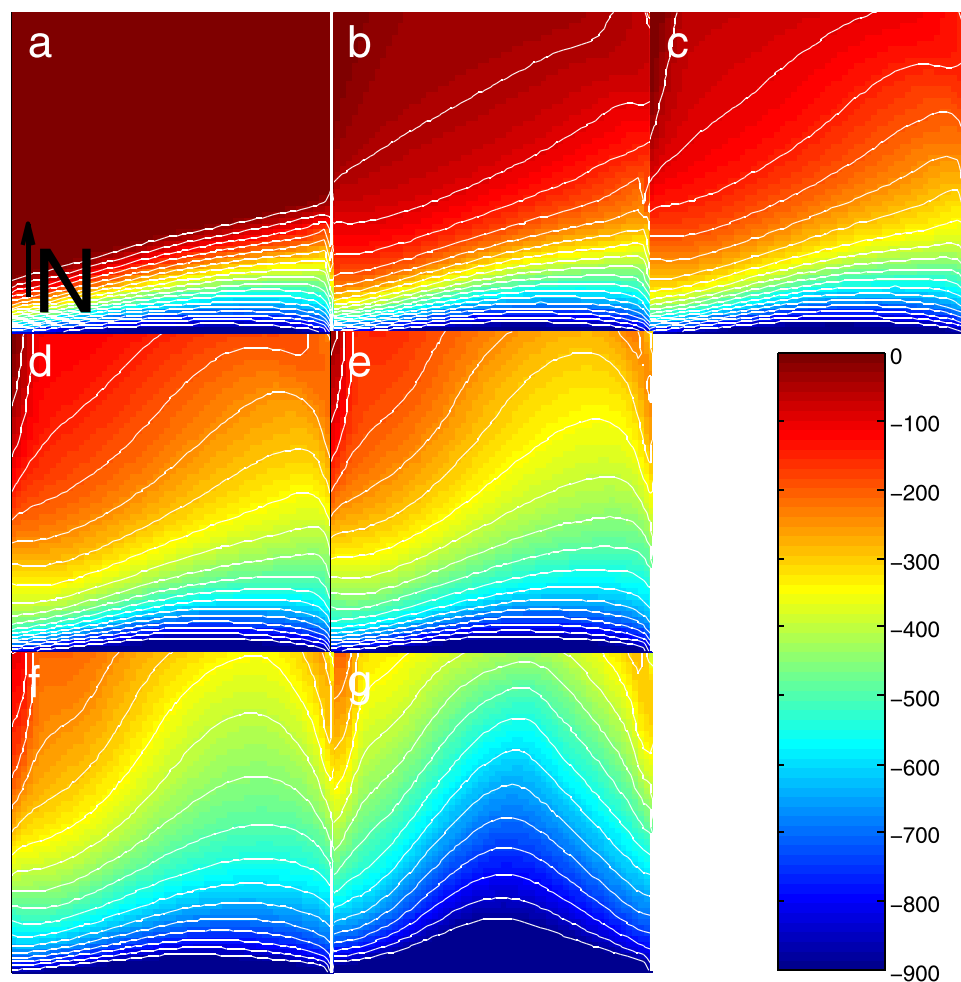


**Figure 9.** (a) Steady state ice-shelf depth (colors, 50 m contours) for the warm, (b) 100 m start of pycnocline depth, (c) 200 m start of pycnocline depth, (d) 300 m start of pycnocline depth, (e) 400 m start of pycnocline depth, (f) 500 m start of pycnocline depth, and (g) cold forcings.

Figure 10a shows the area averaged (depth binned every 20 m) steady state melt rate for the various forcing simulations as a function of depth. Depths less than the minimum thickness of the ice shelf have zero melt rate while maximum melt rates are achieved at a depth just above that of the thickest ice. This is due to the greatest  $u_*$  velocities being located just away from the southern boundary. Melting does not occur below 900 m depth, due to the incoming ice being limited to 900 m depth. Interestingly, despite all cases (except the cold case) having the same maximum thermal forcing they do not have the same maximum melt rate. As melt rate is a function of both thermal driving and  $u_*$ , this would suggest that progressive thinning of the ice shelf by means of a higher pycnocline leads to higher ocean velocities due to a combination of a steepening of the ice-shelf gradient and a stronger meltwater plume. Raising the pycnocline by 100 m sees a reduction in ice-shelf thickness of roughly 40 m at the calving front.

Figure 11 shows the average backstress, and hence buttressing, of the coupled runs as a function of total ice-shelf mass, with warmer runs having both reduced mass and buttressing. Note that in reality this reduced buttressing would lead to a speed up of ice crossing the grounding line, while our model has a constant ice influx over the grounding line. There is a strong correlation between total ice mass and buttressing, with higher ice-shelf mass leading to higher backstress. Raising the pycnocline by 100 m has the effect of reducing backstress by roughly  $0.4 \times 10^9$  N. While the rate of backstress reduction per meter of pycnocline depth remains constant throughout our runs, as a percentage of total back stress this becomes more significant with higher pycnoclines.

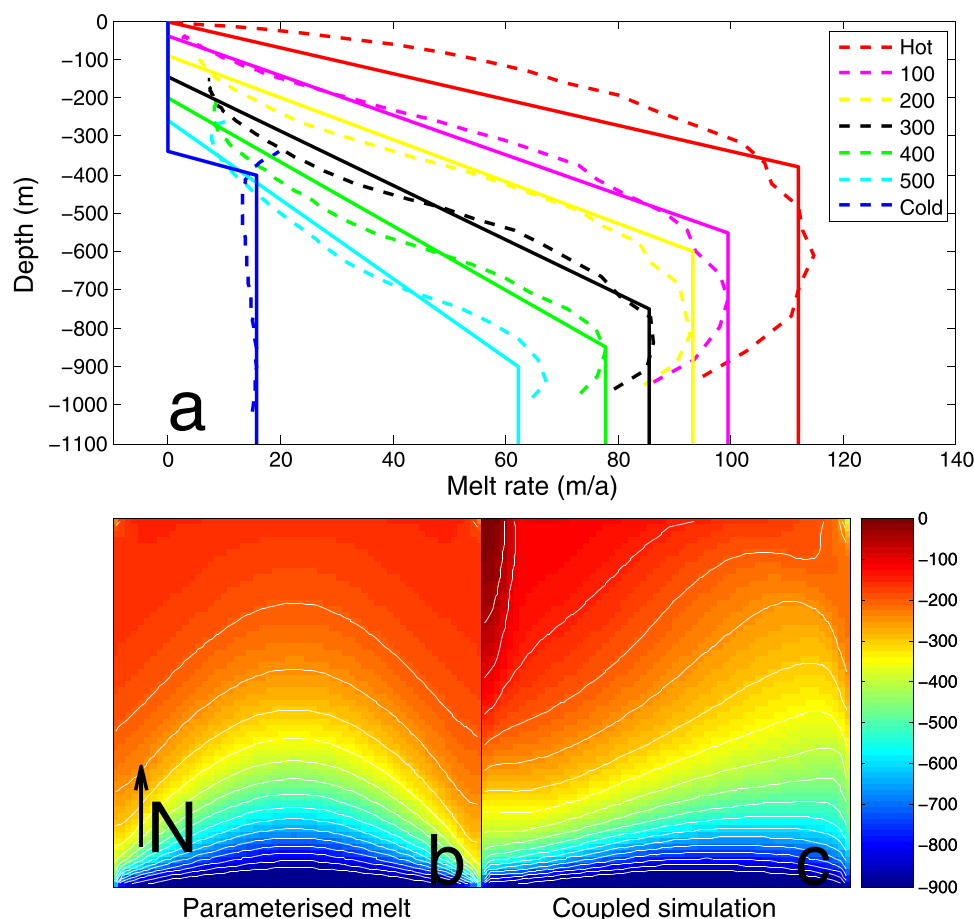


**Figure 10.** (a) Depth averaged mean melt rates (dashed line) and parameterized melt rate (solid line) for the seven forcings using steady state ice-shelf thickness from the coupled model for each individual forcing, (b) steady state ice-shelf depth (colors, 50 m depth contours) for the parameterized melt (ice only model), 300 m start of pycnocline depth simulation, and (c) steady state ice-shelf depth (colors, 50 m depth contours) for the coupled (ice and ocean model), 300 m start of pycnocline depth simulation.

#### 5.4. Comparison of Parameterized Melt and Coupled Model

Finally, we compare our coupled ice shelf-ocean model to an ice only model with no ocean where a typical, depth-dependent melt rate parameterization (Favier et al., 2014; Joughin et al., 2010) has been applied to the ice. Such a parameterization typically has no melting until a particular depth close to the surface (representing the minimum thickness of the ice shelf) and then a linearly increasing melt rate with depth to a maximum melt rate which is maintained for the rest of the profile. Our melt rate parameterizations for each forcing were obtained from the depth averaged (binned every 20 m) melt rates of the steady state coupled simulations. The melt rate profiles are then parameterized as previously described (Figure 10a).

When using a parameterized, depth-dependent melt rate with only the ice component of the model (Figure 10b) instead of the fully coupled model (Figure 10c) there is a marked difference in final ice-shelf thickness. Parameterized melt leads to a symmetrical ice shelf with a central “bulge,” with no Coriolis driven western thinning. This is in direct contrast to the coupled model, which preferentially thins the western side of the ice shelf due to Coriolis driven flow forming a western boundary channel.

Parameterized melt runs also show a strong correlation between ice-shelf mass and backstress (Figure 11). However, for a given ice-shelf mass, parameterized runs have less backstress than coupled runs. In the baseline case, parameterized melt gives a backstress of roughly 75% of the coupled run, with the percentage difference growing greater in cases with higher melting. This difference is due to the parameterized runs having characteristic ice-shelf topography with relatively thin sides and a thicker middle when compared to

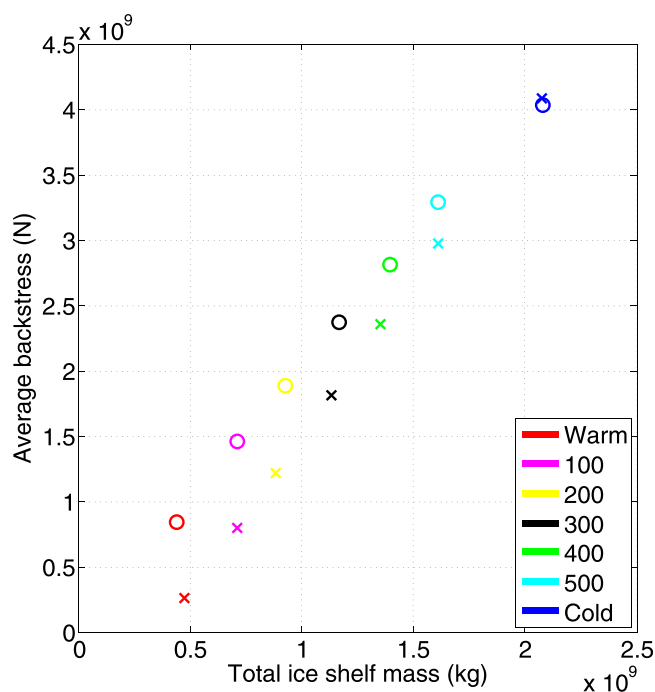


**Figure 11.** Steady state total ice-shelf mass and average backstress for the seven forcing in the coupled (circles) and parameterized melting (cross) simulations

coupled runs. As backstress is predominately determined by ice-shelf mass along the lateral margins of the ice shelf this leads to a lower backstress for a given ice-shelf mass. In the coldest case there is a convergence of the coupled and parameterized runs, as the steady state cold ice-shelf thickness mostly resembles that of a parameterized melt run.

## 6. Discussion and Conclusions

We have presented here the first truly synchronous coupled ice shelf-ocean model, developed using the MITgcm capability to simulate both subice shelf cavity circulation and to simulate coupled ice shelf-ice stream systems. Compared to the previous asynchronous and discontinuous approaches there is no loss of information due to model restarts; the coupling process is fully conservative of mass, heat and salt (or freshwater). Unlike asynchronous coupling approaches it does not suffer from artificial barotropic and baroclinic adjustment processes incurred at each restart. The model can also respond to forcings that vary on a much quicker time scale than some previous approaches. By using the same ocean and ice grid we eliminate the need for averaging and smoothing of the melt rate. The model is being further developed to incorporate grounded ice and a moving grounding line that will allow study of the full ice-ocean system. Large scale calving events, such as the detached iceberg in the warm case (Figure 6), could also be investigated with the addition of a proper calving model.

Coupled simulations for a range of pycnocline depths show the ice shelf progressively thinning on the western boundary, with Coriolis driven flow forming a melt-driven channel. This asymmetry in ice-shelf topography becomes more pronounced with increased melting. This is in direct contrast to uncoupled, ice only runs with a simple melt rate parameterization, which tend to be symmetrical with relatively thin sides with a thicker central “bulge.” While the spatial distribution of mass was different between the two approaches, the total ice-shelf mass for each forcing was accurately reproduced by the ice only simulations. However, this was only achieved by first using the coupled model to derive the melt rate profiles, partly eliminating the need for the melt rate parameterization in the first place. For the simple melt rate parameterization used here to be effective it would, ideally, be able to be used for any given ice-shelf geometry and forcing and produce similar results to a coupled model. Even in the best possible situation (deriving melt rate parameterization from the coupled model) the spatial distribution of ice-shelf mass cannot be reproduced, even if the total ice-shelf mass can be. This is a problem, because ice-shelf backstress is dependent upon the thickness of the ice-shelf at the lateral shear margins. Coupled simulations have thicker ice on average at the margins, with a thin western boundary more than compensated by a thicker eastern boundary. As a direct result of this, when comparing coupled runs to parameterized melt runs there is a significant (roughly 30% in the baseline, 300 m pycnocline depth case) difference in backstress for a given ice-shelf mass, with the uncoupled simulations underestimating buttressing. The presence of a western boundary channel in coupled simulations is likely to become of increased importance once the implementation of a moving grounding line into the model is finished. As the grounding line of an ice-shelf retreats, the lengthening shelf provides a negative feedback to further retreat which can be counteracted by positive feedback from a retrograde bed slope (Goldberg et al., 2012b). A western boundary channel that has melted all the way through may act against this feedback by effectively shortening the length of the ice shelf. The synchronous coupling approach we have developed here would be well suited to further investigate the ice-shelf channels, as their formation is a result of the coupled feedbacks between ice shelf and ocean (Gladish et al., 2012). Goldberg et al. (2012b) were able to produce along-shelf ice-shelf channels with a discontinuous approach, while Sergienko (2013) produced both along-shelf and transverse channels (albeit with a plume model rather than a full ocean model). Transverse channels would lead to high-frequency ice thickness variations as they are advected, leading to the need for a synchronously coupled approach to fully understand the channels and their impact on ice shelves.

One of the problem with the simple method of parameterizing melt rates commonly used (Favier et al., 2014; Joughin et al., 2010) is that, by choosing a depth at which melt rates tend to zero, the minimum thickness of the ice shelf is being arbitrarily forced. As backstress, and hence buttressing, is strongly dependent upon ice-shelf thickness this can lead to inaccurate estimates of buttressing change in response to climate forcing. To make the issue of using parameterized melting more problematic, the maximum melt rate for each of our forcings was found to be different, despite using the same maximum temperature (albeit with a differing position of the pycnocline) in each case. This means that, even if ice-shelf melt rate has been successfully parameterized with a given pycnocline position, the effect of moving the pycnocline upon melt rate is not the same as simply moving the depth of maximum melt rate in the parameterization. The slope of the ice shelf arising from melting affects the melting itself due to a change in the calculation of  $u_*$ . It should be noted that we have only looked at a simple depth-dependent melt rate parameterization. Parameterizing a meltwater plume, such that it takes into account the local ice-shelf slope (Lazeroms et al., 2017), may do a better job of reproducing the coupled models steady state ice-shelf geometry, however it will still be unable to reproduce the Coriolis-enhanced western flow that leads to the western channel formation. Such parameterizations are a recent development, however, and are as yet not widely used.

There is no reason why our approach to synchronous coupling could not be used with other models. For example, the implementation of ice shelves in NEMO (Nucleus for European Modeling of the Ocean) (Mathiot et al., 2017) uses the same pressure loading method of Losch (2008) which, in combination with a nonlinear free surface, forms the basis of our synchronous coupling approach. In addition to our synchronous coupling approach, the changes made to the boundary layer used in melt rate calculations (which greatly reduce, but do not eliminate, the “stripy” melt rates common to z level models) could be used in other z level models. As these changes are completely independent of the coupling process they can freely be used in uncoupled simulations. Finally, the method of model remeshing described here is, with some adjustment of the code, applicable to a number of cases involving a moving boundary between two media; for example sea ice formation or sediment deposition and erosion.

#### Acknowledgments

This work was supported by the UK Natural Environment Research Council under grant NE/M003590/1.

P. Heimbach is supported in part by NSF OCE 1737759 and NASA NNX13AK88G. The newly developed code used throughout this manuscript can be accessed via mitgcm.org.

#### References

- Adcroft, A., Hill, C., & Marshall, J. (1997). Representation of topography by shaved cells in a height coordinate ocean model. *Monthly Weather Review*, 125(9), 2293–2315. [https://doi.org/10.1175/1520-0493\(1997\)125<2293:ROTBSC>2.0.CO;2](https://doi.org/10.1175/1520-0493(1997)125<2293:ROTBSC>2.0.CO;2)
- Asay-Davis, X. S., Cornford, S. L., Durand, G., Galton-Fenzi, B. K., Gladstone, R. M., Gudmundsson, G. H., . . . Seroussi, H. (2016). Experimental design for three interrelated marine ice sheet and ocean model intercomparison projects: Mismip v. 3 (mismip+), isomip v. 2 (isomip+) and misomip v. 1 (misomip1). *Geoscientific Model Development*, 9(7), 2471–2497. <https://doi.org/10.5194/gmd-9-2471-2016>
- Campin, J.-M., Adcroft, A., Hill, C., & Marshall, J. (2004). Conservation of properties in a free-surface model. *Ocean Modelling*, 6(3–4), 221–244. [https://doi.org/10.1016/S1463-5003\(03\)00009-X](https://doi.org/10.1016/S1463-5003(03)00009-X)
- De Rydt, J., & Gudmundsson, G. H. (2016). Coupled ice shelf-ocean modeling and complex grounding line retreat from a seabed ridge. *Journal of Geophysical Research: Earth Surface*, 121, 865–880. <https://doi.org/10.1002/2015JF003791>
- De Rydt, J., Holland, P. R., Dutrieux, P., & Jenkins, A. (2014). Geometric and oceanographic controls on melting beneath Pine Island Glacier. *Journal of Geophysical Research: Oceans*, 119, 2420–2438. <https://doi.org/10.1002/2013JC009513>
- Depoorter, M. A., Bamber, J. L., Griggs, J. A., Lenaerts, J. T. M., Ligtenberg, S. R. M., van den Broeke, M. R., & Moholdt, G. (2013). Calving fluxes and basal melt rates of Antarctic ice shelves. *Nature*, 502, 89–92. <https://doi.org/10.1038/nature12567>
- Dupont, T., & Alley, R. (2005). Assessment of the importance of ice-shelf buttressing to ice-sheet flow. *Geophysical Research Letters*, 32, L04503. <https://doi.org/10.1029/2004GL022024>
- Dutrieux, P., De Rydt, J., Jenkins, A., Holland, P. R., Ha, H. K., Lee, S. H., . . . Schröder, M. (2014). Strong sensitivity of Pine Island Ice-Shelf melting to climatic variability. *Science*, 343(6167), 174–178. <https://doi.org/10.1126/science.1244341>
- Favier, L., Durand, G., Cornford, S. L., Gudmundsson, H. G., Gagliardi, O., Gillet-Chaulet, F., . . . Brocq, A. M. L. (2014). Retreat of Pine Island Glacier controlled by marine ice-sheet instability. *Nature Climate Change*, 4(2), 336–348. <https://doi.org/10.1038/nclimate2094>
- Gladish, C. V., Holland, D. M., Holland, P. R., & Price, S. F. (2012). Ice-shelf basal channels in a coupled ice/ocean model. *Journal of Glaciology*, 58(212), 1227–1244. <https://doi.org/10.3189/2012JG12J003>
- Goldberg, D., & Heimbach, P. (2013). Parameter and state estimation with a time-dependent adjoint marine ice sheet model. *The Cryosphere*, 7(6), 1659–1678.
- Goldberg, D. N., Little, C. M., Sergienko, O. V., Gnanadesikan, A., Hallberg, R., & Oppenheimer, M. (2012a). Investigation of land ice-ocean interaction with a fully coupled ice-ocean model. 1: Model description and behavior. *Journal of Geophysical Research: Earth Surface*, 117, F02037. <https://doi.org/10.1029/2011JF002246>
- Goldberg, D. N., Little, C. M., Sergienko, O. V., Gnanadesikan, A., Hallberg, R., & Oppenheimer, M. (2012b). Investigation of land ice-ocean interaction with a fully coupled ice-ocean model. 2: Sensitivity to external forcings. *Journal of Geophysical Research: Earth Surface*, 117, F02038. <https://doi.org/10.1029/2011JF002247>
- Greenbaum, J. S., Blankenship, D. D., Young, D. A., Richter, T. G., Roberts, J. L., Aitken, A. R. A., . . . Siegart, M. J. (2015). Ocean access to a cavity beneath Totten Glacier in East Antarctica. *Nature Geoscience*, 8, 294–298. <https://doi.org/10.1038/ngeo2388>
- Gudmundsson, H. G. (2006). Fortnightly variations in the flow velocity of rutford ice stream, west Antarctica. *Nature*, 444, 1063–1064. <https://doi.org/10.1038/nature05430>
- Jacobs, S., Helmer, H. H., Doake, C. S. M., Jenkins, A., & Frolich, R. M. (1992). Melting of ice shelves and the mass balance of Antarctica. *Journal of Glaciology*, 38(130), 375–387.

- Jacobs, S. S., Hellmer, H. H., & Jenkins, A. (1996). Antarctic Ice Sheet melting in the southeast Pacific. *Geophysical Research Letters*, *23*(9), 957–960. <https://doi.org/10.1029/96GL00723>
- Jenkins, A., Dutrieux, P., Jacobs, S. S., McPhail, S. D., Perrett, J. R., Webb, A. T., & White, D. (2010). Observations beneath Pine Island Glacier in West Antarctica and implications for its retreat. *Nature Geoscience*, *3*, 468–472. <https://doi.org/10.1038/ngeo890>
- Jenkins, A., Hellmer, H. H., & Holland, D. M. (2001). The role of meltwater advection in the formulation of conservative boundary conditions at an ice-ocean interface. *Journal of Physical Oceanography*, *31*(1), 285–296. [https://doi.org/10.1175/1520-0485\(2001\)031<0285:TROMAI>2.0.CO;2](https://doi.org/10.1175/1520-0485(2001)031<0285:TROMAI>2.0.CO;2)
- Joughin, I., Alley, R. B., & Holland, D. M. (2012). Ice-sheet response to oceanic forcing. *Science*, *338*(6111), 1172–1176. <https://doi.org/10.1126/science.1226481>
- Joughin, I., Smith, B. E., & Holland, D. M. (2010). Sensitivity of 21st century sea level to ocean-induced thinning of pine island glacier, Antarctica. *Geophysical Research Letters*, *37*, L20502. <https://doi.org/10.1029/2010GL044819>
- Lazeroms, W. M. J., Jenkins, A., Gudmundsson, G. H., & van de Wal, R. S. W. (2017). Modelling present-day basal melt rates for Antarctic ice shelves using a parametrization of buoyant meltwater plumes. *The Cryosphere Discussions*, *2017*, 1–29. <https://doi.org/10.5194/tc-2017-58>
- Losch, M. (2008). Modeling ice shelf cavities in a z coordinate ocean general circulation model. *Journal of Geophysical Research: Oceans*, *113*, C08043. <https://doi.org/10.1029/2007JC004368>
- MacAyeal, D. R. (1989). Large-scale ice flow over a viscous basal sediment: Theory and application to ice stream b, Antarctica. *Journal of Geophysical Research*, *94*(B4), 4071–4087. <https://doi.org/10.1029/JB094iB04p04071>
- Marshall, J., Hill, C., Perelman, L., & Adcroft, A. (1997). Hydrostatic, quasi-hydrostatic, and nonhydrostatic ocean modeling. *Journal of Geophysical Research*, *102*(C3), 5733–5752. <https://doi.org/10.1029/96JC02776>
- Mathiot, P., Jenkins, A., Harris, C., & Madec, G. (2017). Explicit and parametrised representation of under ice shelf seas in a z\* coordinate ocean model. *Geoscientific Model Development Discussions*, *2017*, 1–43. <https://doi.org/10.5194/gmd-2017-37>
- Pattyn, F., & Durand, G. (2013). Why marine ice sheet model predictions may diverge in estimating future sea level rise. *Geophysical Research Letters*, *40*, 4316–4320. <https://doi.org/10.1002/grl.50824>
- Petty, A. A., Feltham, D. L., & Holland, P. R. (2013). Impact of atmospheric forcing on Antarctic continental shelf water masses. *Journal of Physical Oceanography*, *43*(5), 920–940. <https://doi.org/10.1175/JPO-D-12-0172.1>
- Scambos, T. A., Bohlander, J. A., Shuman, C. A., & Skvarca, P. (2004). Glacier acceleration and thinning after ice shelf collapse in the Larsen B embayment, Antarctica. *Geophysical Research Letters*, *31*, L18402. <https://doi.org/10.1029/2004GL020670>
- Sergienko, O. V. (2013). Basal channels on ice shelves. *Journal of Geophysical Research: Earth Surface*, *118*, 1342–1355. <https://doi.org/10.1002/jgrf.20105>
- Seroussi, H., Nakayama, Y., Larour, E., Menemenlis, D., Morlighem, M., Rignot, E., & Khazendar, A. (2017). Continued retreat of thwaites glacier, west Antarctica, controlled by bed topography and ocean circulation. *Geophysical Research Letters*, *44*, 6191–6199. <https://doi.org/10.1002/2017GL072910>
- Shepherd, A., Wingham, D., & Rignot, E. (2004). Warm ocean is eroding West Antarctic Ice Sheet. *Geophysical Research Letters*, *31*, L23402. <https://doi.org/10.1029/2004GL021106>
- Silvano, A., Rintoul, S. R., & Herraiz-Borreguero, L. (2016). Ocean-ice shelf interaction in east Antarctica. *Oceanography*, *29*, 130–143.
- Smith, B. E., Gourmelen, N., Huth, A., & Joughin, I. (2017). Connected subglacial lake drainage beneath thwaites glacier, west Antarctica. *The Cryosphere*, *11*(1), 451–467. <https://doi.org/10.5194/tc-11-451-2017>
- Thomas, R. H. (1979). The dynamics of marine ice sheets. *Journal of Glaciology*, *24*(90), 167–177. <https://doi.org/10.3198/1979JoG24-90-167-177>
- Thomas, R. H., Sanderson, T. J. O., & Rose, K. E. (1979). Effect of climatic warming on the West Antarctic Ice Sheet. *Nature*, *277*, 355–358. <https://doi.org/10.1038/277355a0>
- Walker, D. P., Brandon, M. A., Jenkins, A., Allen, J. T., Dowdeswell, J. A., & Evans, J. (2007). Oceanic heat transport onto the Amundsen sea shelf through a submarine glacial trough. *Geophysical Research Letters*, *34*, L02602. <https://doi.org/10.1029/2006GL028154>
- Walker, R. T., & Holland, D. M. (2007). A two-dimensional coupled model for ice shelf-ocean interaction. *Ocean Modelling*, *17*(2), 123–139. <https://doi.org/10.1016/j.ocemod.2007.01.001>